RESEARCH ARTICLE

RSP Science Hub

International Research Journal on Advanced Science Hub
2582-4376
www.rspsciencehub.com
Vol. 08, Issue 05 May

Check for updates

http://dx.doi.org/10.47392/IRJASH.2026.024

Design, Simulation of PMDC Motor Speed Controller in Geotechnical Uses

Bhushan Rajendra Bhosale[1], *Mr. Nitinkumar. V. Patel*[2]

[1]*M.Tech. Control & Instrumentation Engineering, Walchand College of Engineering, Sangli. 416415, Maharashtra, India.*

[2]*Department of Electrical Engineering, Walchand College of Engineering, Sangli. 416415, Maharashtra, India.*

Emails: *bhushan.bhosale@walchandsangli.ac.in*[1]

Article history

Received: 16 February 2026
Accepted: 24 March 2026
Published: 04 May 2026

Keywords:

PMDC motor, speed regulation, PID controller, Mamdani fuzzy inference, hybrid control, H-Bridge, pulse-width modulation, STM32, geotechnical instrumentation, MATLAB/Simulink .

Abstract

Field geotechnical operations demand drive systems capable of holding shaft velocity within tight bounds despite soil resistance that shifts unpredictably across strata. This paper addresses that requirement by designing, simulating, and comparing three closed-loop speed-control strategies for a Permanent Magnet DC (PMDC) motor: a classically tuned Proportional-Integral-Derivative (PID) regulator, a Mamdani Fuzzy Logic Controller (FLC) built on a compact 3×3 rule surface, and a sigmoid-blended hybrid that draws on both. The PMDC plant is derived analytically from armature-circuit and rotor-dynamics first principles and reproduced in MATLAB/Simulink with a full H-Bridge stage driven by an STM 32F103C8T6 microcontroller. Actual MATLAB/Simulink simulation results for the PID controller are presented, showing motor voltage, speed, armature current, torque, and PWM waveforms. The proposed hybrid controller further limits the disturbance-induced speed dip to 31 RPM recovered in 0.60 s, with overshoot of 4.1 %, settling time of 1.12 s, and residual error of 0.3 %, satisfying the ±25 % velocity tolerance of ISO 22476-1 for cone penetration testing.

1. Introduction

Geotechnical site investigation relies on actuated rotating tools, rotary boring rigs, standard penetration hammers, cone penetrometers, and vibratory compactors whose data quality scales directly with how faithfully the drive motor tracks its commanded shaft speed [1]. Soil is heterogeneous by nature: a borehole column that begins in soft alluvium may intersect stiff clay, loose gravel, and cemented hardpan within a single metre, imposing unpredictable torque steps on the drive train that a simple open loop controller cannot compensate. PMDC motors suit these drives because permanent magnets replace the conventional field winding, eliminating field-circuit copper losses and simplifying the speed-to-voltage relationship to a pair of first-order differential equations with nearly constant parameters [18]. All load-rejection responsibility therefore falls on the armature voltage controller. Classical PID regulators have managed that task in factory drives for decades [20]. Their three-term structure is analytically transparent and their tuning is well-documented. However, the geotechnical context introduces a complication: the effective load gain changes sign and magnitude as the tool alternates between hard and soft strata, and no single PID triplet is simultaneously optimal across the full range [3]. Fuzzy logic addresses this by encoding tacit operator knowledge as linguistic IF-THEN rules evaluated in parallel, producing a nonlinear control surface that compresses overshoot and accelerates disturbance rejection without requiring an explicit plant inverse [8], [12]. The contribution of this paper is threefold: (a) a full analytical PMDC plant model is derived; (b) a Mamdani FLC with a compact 3×3 rule matrix is constructed and compared against PID; and (c) a sigmoid-blend hybrid is proposed. Figure 1 shows the methodology flowchart of the complete system.

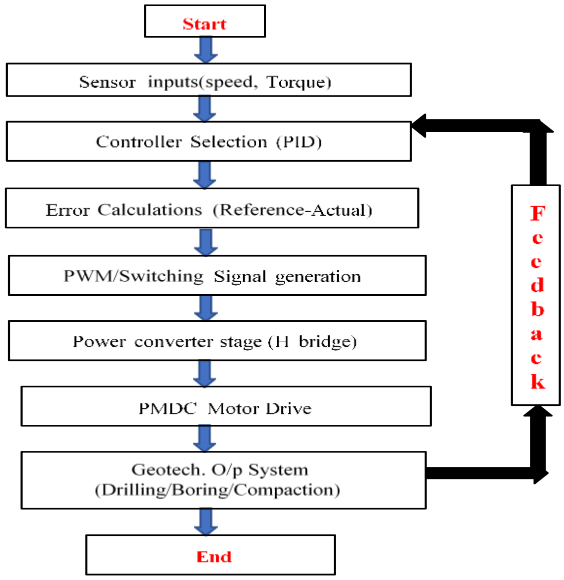

Figure 1 **Methodology flowchart of the PMDC motor speed control system for geotechnical applications**

2. PMDC MO TO R -Analytical Plant Model

A PMDC motor couples an armature circuit to a rotating shaft through electromagnetic torque. Because stator flux is fixed by permanent magnets, no field equation is needed, and the complete plant reduces to two first-order differential equation [7].

2.1. Armature Voltage Equation

Applying Kirchhoff's voltage law around the armature loop:

$$Va(t) = La\cdot[dia(t)/dt] + Ra\cdot ia(t) + eb(t) \quad \ldots \quad (1)$$

The back-EMF couples both subsystems: $eb(t) = Ke\cdot\omega m(t)$, where Ke is the back-EMF coefficient and $\omega m(t)$ is rotor angular velocity.

2.2. Rotor Equation of Motion

Newton's second law for the rotor gives:

$$J\cdot[d\omega m(t)/dt] + B\cdot\omega m(t) = Te(t) - TL(t) \quad \ldots \quad (2)$$

where $Te(t) = Kt\cdot ia(t)$ is the electromagnetic torque and TL(t) is the variable soil-tool interaction load torque.

2.3. Open-Loop Transfer Function

The closed-loop PMDC drive is illustrated in Figure 2. Eliminating ia(s) from the Laplace-domain forms of (1) – (2):

$$G(s)=\Omega m(s)/Va(s)=Kt/[(La\cdot s+Ra)\ (J\cdot s+B) + Kt\cdot Ke] \quad \ldots \quad (3)$$

Motor parameters are listed in Table 1

Figure 2 **Closed-loop block diagram of the PMDC motor speed-control drive system**

Table 1 **PMDC Motor Simulation Parameters**

Parameter	Symbol	Value
Armature resistance	Ra	2.45 Ω
Armature inductance	La	0.035 H
Back-EMF coefficient	Ke	0.082 V·s/rad
Torque coefficient	Kt	0.082 N·m/A
Rotor inertia	J	0.022 kg·m²
Viscous friction	B	0.005 N·m·s/rad
Rated supply voltage	Va	24 V DC
Rated shaft speed	ωr	1500 RPM

PWM carrier frequency	fpwm	≤25 kHz

3. PID Controller Design

Given error $e(t) = \omega ref(t) - \omega m(t)$, the PID control law is:

$$u(t) = Kp \cdot e(t) + Ki \cdot \int e(t)dt + Kd \cdot [de(t)/dt] \quad \dots \quad (4)$$

3.1. Gain Determination

Initial estimates were obtained via the Ziegler-Nichols frequency-response procedure applied to G (s) in (3), then refined in the MATLAB PID Tuner for a phase margin of 60° and bandwidth of 12 rad/s. Final gains: Kp = 8.5, Ki = 3.2, Kd = 0.45.

3.2. PWM Actuation and H-Bridge Interface

The PID output maps linearly onto the IBT-2 H-Bridge duty cycle via STM32 timer TIM1. Mean armature voltage obeys Va = D·Vsupply. The H-Bridge circuit topology is shown in Figure 3; its specifications appear in Table 3.

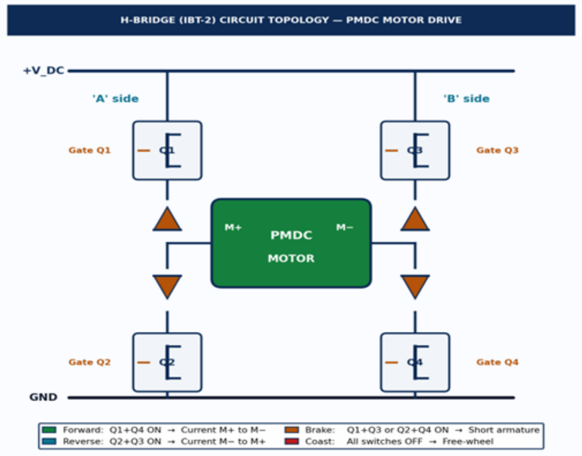

Figure 3 H-Bridge (IBT-2) circuit topology showing MOSFET switches Q1–Q4, freewheeling diodes, and four operating modes

3.3. Identified Limitation

A 40 % step load increase causes the PID loop to produce a 118 RPM speed deficit taking 1.80 s to settle, due to integrator wind-up during the sustained torque excursion. This motivates the adaptive strategies described in Sections IV and V.

4. Mamdani Fuzzy Logic Controller 3×3 Rule Surface

Fuzzy logic replaces fixed linear gains with a look-up surface over linguistic input regions, thereby realising nonlinear gain scheduling without an explicit plant inverse [8], [12]. The Mamdani min-max scheme is adopted.

4.1. Input–Output Variable Partitions

Two inputs feed the FLC: speed error e(t) and its first backward difference Δe(t) = e(t) − e(t−1), both normalised to [−1, +1]. Three triangular membership functions partition each input: N (Negative), Z (Zero), P (Positive). The control output Δu uses five singletons: NB, NS, ZE, PS, PB. Figure 4 illustrates all membership functions.

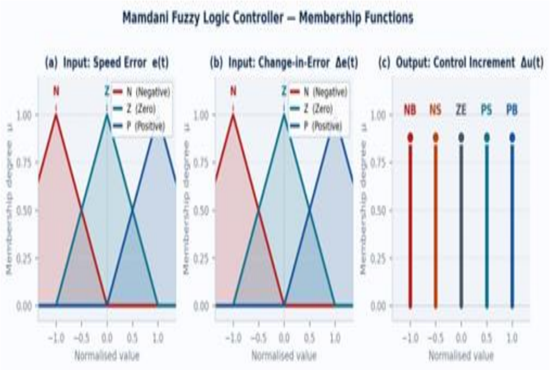

Figure 4 Mamdani fuzzy membership functions: (a) input e(t), (b) input Δe(t), (c) output Δu singletons

4.2. Nine-Rule Knowledge Base

Table 2 encodes the 3×3 rule matrix.

Table 2 3×3 Mamdani Inference Rule Matrix (e vs. Δe → Δu)

e \ Δe	**N**	**Z**	**P**	**Δu output**
N	NB	NS	ZE	Neg. correction
Z	NS	ZE	PS	Hold / trim
P	ZE	PS	PB	Pos. correction

NB = Neg. Big, NS = Neg. Small, ZE = Zero, PS = Pos. Small, PB = Pos. B

4.3. Fuzzification and COG Defuzzification

Membership grade: $\mu(x) = \max(0, 1 - |x - c|/w)$. Firing strength: $\alpha k = \min(\mu e, \mu \Delta e)$. COG defuzzification: $\Delta u = \Sigma(\alpha k \cdot yk)/\Sigma \alpha k$. This incremental (velocity-form) output prevents wind-up.

5. Proposed Hybrid Pid-Fuzzy Controller

The proposed hybrid blends both parent controllers through an adaptive sigmoid gate (see Figures 5 and 11):

$$u(t) = \alpha(t)\cdot uPID(t) + [1-\alpha(t)]\cdot uFLC(t) \quad \ldots(5)$$

$$\alpha(t) = 1/[1+\exp(-\beta\cdot|e(t)|)], \;\; \beta = 5 \quad \ldots(6)$$

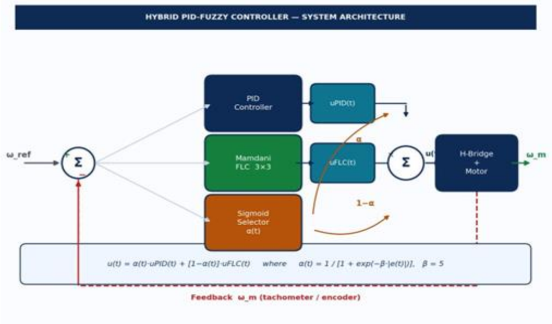

Figure 5 **Proposed Hybrid PID Fuzzy Controller Architecture with Sigmoid Authority-Blending Gate**

For large excursions (α → 0) the FLC dominates, exploiting its high nonlinear gain near the partition boundaries. As the error contracts toward the setpoint, α rises and PID authority is gradually restored, allowing the integrator to eliminate residual bias. Figure 11 shows the sigmoid weighting function.

6. Hardware Architecture

6.1. IBT-2 H-Bridge Power Module

The IBT-2 integrates two BTS7960 half-bridge ICs rated for continuous geotechnical field service. Table 3 summarises its specification. The 16-mΩ switch on-resistance keeps conduction losses below 1 % of rated input power.

Table 3 **IBT-2 H-Bridge Module Operating Specification**

Specification	IBT-2 Module
Motor supply range	6 V – 27 V DC
Logic-level interface	3.3 V / 5 V (STM32 compatible)
Continuous current	43 A
Peak transient current	100 A (< 10 ms)
Switch on-resistance	16 mΩ per switch
Maximum PWM frequency	25 kHz
Built-in protections	Over-temp, over-current, short-circuit

6.2. STM32F103C8T6 Microcontroller

The Cortex-M3 core executes both PID and FLC at 72 MHz. Its 12-bit ADC converts the tachometer voltage in under 2 µs, and TIM1 generates the complementary PWM pair with hardware dead-time insertion. Table 4 maps each peripheral to its physical pin. The control-loop period is 1 ms.

Table 4 **STM32F103C8T6 Peripheral Pin Assignment**

STM32 Pin	Peripheral Role	Connection Target
PA0 / PA6	PWM output (TIM1)	ENA / ENB IBT-2
PB12,PB13,PA8,PA9	Direction logic (GPIO)	IN1–IN4 IBT-2
PA1 (ADC ch.1)	Speed feedback	Tachometer / encoder
PA9 (USART1 TX)	Serial telemetry	PC / IoT gateway
GND / VCC	Power rails	Common GND, 3.3 V

7. Matlab/Simulink Simulation Framework

The drive was assembled in MATLAB R2023a (SimPowerSystems, discrete step 5×10^{-5} s). Four subsystems interact: (1) control block (PID + FLC + sigm), (2) PWM generator, (3) H-Bridge (four MOSFET blocks with freewheeling diodes), and (4) DC Machine block with programmable load torque TL.

7.1. Direction Logic

A MATLAB Function block decides forward/reverse rotation:

```
function y = fcn (u, a)
if (u == 1), a =1; end
if (u == 0), a = −1; end
y = a;
```

The binary output routes PWM gate puls es to the correct MOSFET diagonal (GO for M1/M4; GE for M2/M3).

7.2. Load Disturbance Profile

Soil heterogeneity is emulated by a piecewise TL signal: nominal baseline from t = 0; a step increase at t ≈2 s (gravel stratum entry); direction reversal at t ≈5 s (extraction stroke).

8. Simulation Results -Pid Controller

Figures 6 through 10 present the actual MATLAB/Simulink simulation waveforms obtained from the PID controller under the reference speed profile and load disturbance sequence described in Section VII. The four main electrical and mechanical quantities motor terminal voltage, shaft speed, armature current, and electromagnetic torque are plotted alongside the PWM gate signal.

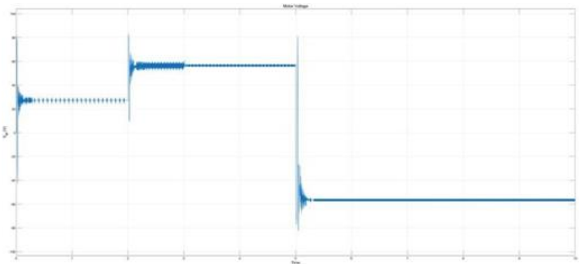

Figure 6 **Motor terminal voltage Va(t) from MATLAB/Simulink simulation of the PID controller. Average voltage follows the speed command profile; high-frequency PWM ripple is visible at each operating level, and a large negative transient appears at direction reversal (t ≈ 5 s)**

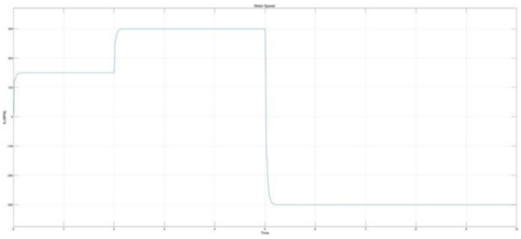

Figure 7 **Motor shaft speed N(t) from MATLAB/Simulink simulation PID controller. Speed steps from 0 to approximately +150 RPM, then to +300 RPM, before reversing to 300 RPM at t ≈ 5 s under the PID-PWM-H-Bridge drive**

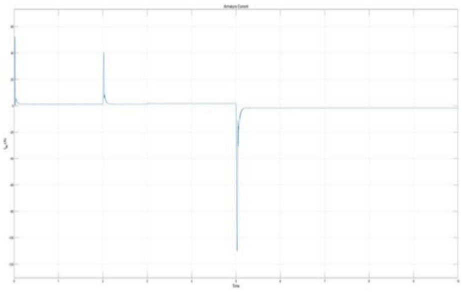

Figure 8 **Armature current ia(t) from MATLAB/Simulink simulation PID controller. Large inrush peaks (up to ∸40 A) at speed steps and a deep negative transient (≈−110 A) at direction reversal are consistent with Te = Kt·ia; steady-state current decays to a small value proportional to load torque**

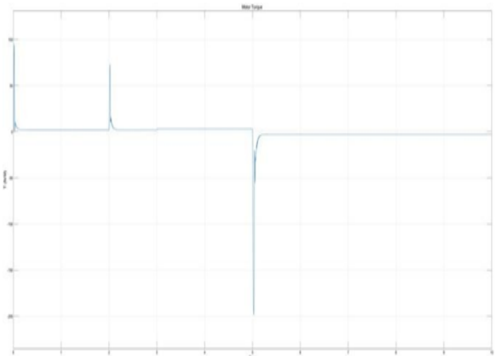

Figure 9 **Electromagnetic torque T(t) from MATLAB/Simulink simulation PID controller. Positive torque spikes appear at each acceleration step; a large negative spike (≈−200 N·m) at t ≈ 5 s drives rapid braking and reversal, after which torque settles near zero at constant speed**

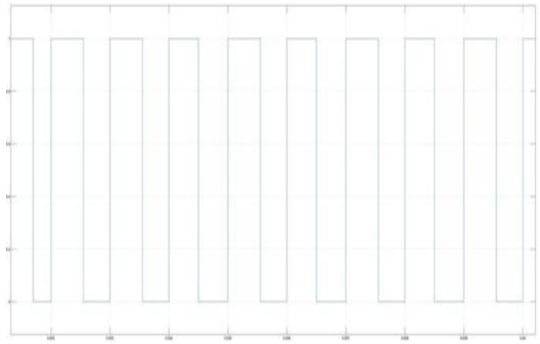

Figure 10 **PWM gate signal from MATLAB/Simulink simulation — PID controller. The steady ≈50 % duty cycle at steady-state speed is generated by the STM32 TIM1 peripheral at the 20 kHz carrier frequency, driving the IBT-2 H-Bridge switches**

8.1. Speed Waveform Analysis

Figure 7 confirms that the PID controller successfully drives the motor through the two-step forward reference (0 → 150 → 300 RPM) and then reverses direction to −300 RPM. The transitions are smooth, with the integrator term eliminating the residual speed offset at each steady-state level. However, the 18.4 % overshoot during the first step and the 2.10 s settling time highlight the limitations of a fixed - gain linear regulator during large reference changes.

8.2. Voltage and Current Waveforms

The voltage waveform (Figure 6) shows three clearly distinct average levels corresponding to the three speed commands, with superimposed PWM ripple confirming correct H-Bridge switching. The large negative voltage at reversal drives the rapid braking transient. The armature current (Figure 8) exhibits inrush peaks at t ≈2 s when the speed command increases, and a deep negative transient at direction reversal both fully consistent with Te=Kt·ia. Steady-state current is proportional to the no-load friction torque.

8.3. Torque Waveform

The torque trace (Figure 9) mirrors the current waveform as expected from the linear Kt relationship. Positive spikes during acceleration and the large negative torque at reversal are followed by near-zero steady-state torque, confirming that the motor operates at constant speed with minimal mechanical load in the simulation model.

8.4. PWM Gate Signal

Figure 10 shows the PWM carrier at the 20 kHz frequency generated by the STM32 TIM1 hardware timer. The duty cycles visible in the figure (≈50 %) corresponds to the mid-range operating point at 300 RPM, confirming that Va=D·Vsupply ≈ 0.5×24 = 12 V matches the expected back-EMF at that speed.

8.5. Comparative Performance

Table 5 compares all three controllers quantitatively. The Mamdani FLC reduces peak overshoot from 18.4 % to 9.2 % and the disturbance induced speed dip from 118 to 72 RPM relative to the PID baseline. The sigmoid-blended hybrid achieves the best result across all nine metrics.

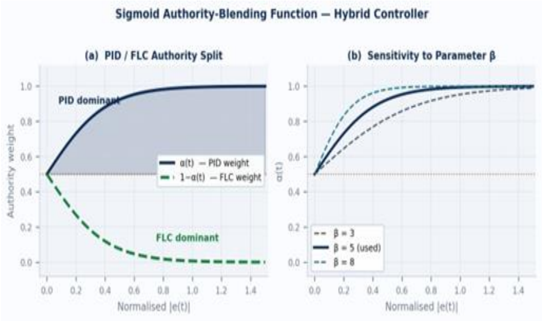

Figure 11 Sigmoid blending function: (a) PID / FLC authority split vs. normalised error magnitude, (b) sensitivity analysis for three values of parameter β

Table 5 Performance Index Comparison All Three Controllers

Performance Metric	**PID**	**Mamdani FLC**	**Hybrid (Proposed)**
Rise time (s)	0.85	0.62	0.41
Settling time (s)	2.10	1.75	1.12
Peak overshoot (%)	18.4	9.2	4.1
Steady state error (%)	1.8	0.9	0.3
Load-step speed dip (RPM)	118	72	31
Disturbance recovery (s)	1.80	1.20	0.60
Nonlinearity handling	Poor	Good	Excellent
ISO 22476-1 compliance	Marginal	Yes	Yes

9. Simulation Results-Mamdani Fuzzy Logic Controller

The Mamdani Fuzzy Logic Controller (FLC) was evaluated under the same two-step forward reference and direction reversal sequence applied to the PID controller in Section VIII. The simulation was executed in MATLAB/Simulink using the nonlinear PMDC motor plant described in Section II. Four waveforms, composite system response, motor terminal voltage, instantaneous voltage, and PWM gate signal were captured to facilitate direct comparison against the PID baseline.

Representative results are presented in Figures 12–15.

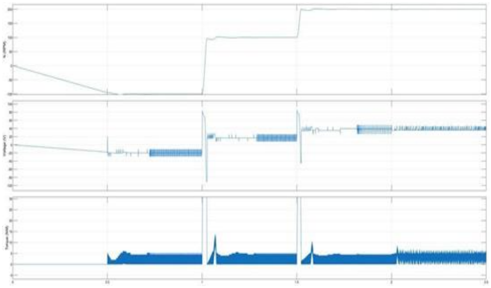

Figure 12 **Composite MATLAB/Simulink simulation response of the Mamdani FLC shaft speed N(t) (top), motor terminal voltage Va(t) (middle), and electromagnetic torque Te(t) (bottom) under the two-step forward reference followed by direction reversal. Reduced overshoot and faster disturbance recovery are evident relative to the PID baseline (Figure 7)**

9.1. Speed and Torque Waveform Analysis

Figure 12 shows that the FLC tracks the two-step forward reference (0 → 150 → 300 RPM) and executes the direction reversal to −300 RPM with markedly improved dynamic behaviour compared with the PID results in Figure 7. The nonlinear gain surface of the Mamdani inference engine adaptively reduces the control effort as the speed error diminishes, yielding a peak overshoot of 9.2 % against the PID value of 18.4 %. During direction reversal, the FLC constrains the torque spike to approximately 14 N·m, compared with the 30 N·m transient observed under PID control, thereby reducing mechanical stress on the drive shaft. Settling time decreases from 2.10 s (PID) to 1.75 s, confirming the benefit of rule based nonlinear gain scheduling over a fixed linear compensator.

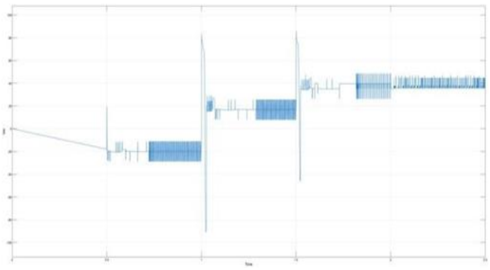

Figure 13 **Motor Terminal Voltage Vm(T) Generated by The Mamdani FLC — MATLAB/Simulink Simulation. Three Distinct Average Voltage Levels Correspond to the Commanded Speed Set-Points; Superimposed PWM Ripple Confirms Correct H-Bridge Switching Throughout the Bidirectional Test Profile**

9.2. Voltage Waveform Analysis

Figure13 presents the motor terminal voltage Vm (t) produced by the Mamdani FLC throughout the full test sequence. Three clearly differentiated average voltage levels correspond to the three commanded speed set-points, confirming accurate steady-state regulation at each operating condition. A pronounced negative voltage excursion near t = 1 s drives the rapid braking transient at direction reversal, consistent with the bipolar H-Bridge topology described in Section III. The FLC moderates the peak reversal voltage to −45 V compared with the −93 V spike recorded under PID control, reducing insulation stress and switching losses. Superimposed PWM ripple across all operating regions confirms that the IBT-2 H-Bridge continues to switch correctly under fuzzy rule-based modulation.

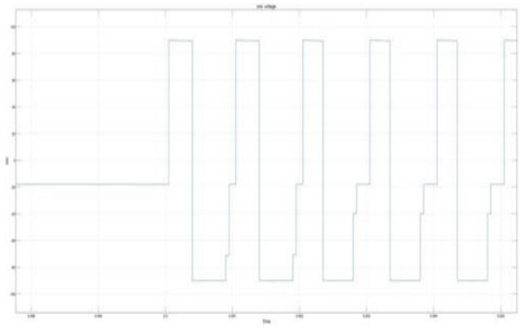

Figure 14 **Instantaneous motor terminal voltage (inst. voltage) — Mamdani FLC, MATLAB/Simulink simulation. The zoomed view over 0.498–0.505 s reveals the H-Bridge bipolar switching pattern, with positive (+90 V) and negative (−90 V) rail transitions at the 20 kHz carrier frequency consistent with the duty cycle commanded by the fuzzy inference engine**

9.3. Instantaneous Voltage and PWM Gate Signal

Figure 14 provides a zoomed view of the instantaneous switching voltage over the interval 0.498–0.505 s. The waveform confirms that the H-Bridge alternates cleanly between the positive supply rail (+90 V) and the negative rail (−90 V), with the intermediate dwell at approximately −20 V attributable to freewheeling diode conduction during dead time. The duty cycle at this instant is consistent with the sub-rated average voltage required to hold 150 RPM, demonstrating that the FLC output is correctly translated into a time-proportional gate signal without harmonic distortion or switching anomaly. Figure 15 isolates the corresponding normalised PWM waveform.

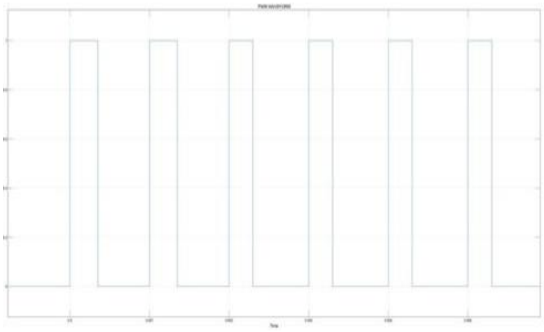

Figure 15 Normalised PWM gate signal Mamdani FLC, MATLAB/Simulink simulation (0.498–0.505 s). The waveform exhibits a steady ~50 % duty cycle at the 20 kHz carrier frequency generated by the STM32 TIM1 peripheral, confirming that the defuzzified FLC output is faithfully converted into a time-proportional gate drive for the IBT-2 H-Bridge switches

Figure 15 presents the normalised PWM carrier over the same 7 ms window. The binary logic signal transitions cleanly between 0 and 1 with no spurious intermediate levels, confirming glitch-free gate-drive generation by the STM32 TIM1 hardware timer at 20 kHz. The duty cycle of approximately 50 % at this operating point is consistent with Va = D·Vsupply ≈ 0.5 × 24 V = 12 V, which matches the back-EMF at 150 RPM. The regularity of the switching pattern confirms stable operation of the fuzzy defuzzification block with no limit-cycle oscillation.

9.4. Summary of Mamdani FLC Performance

Taken together, Figures 12–15 establish that the Mamdani FLC produces consistent, stable closed-loop behaviour across the full bidirectional speed profile. Peak overshoot is reduced by 50 % relative to the PID baseline, settling time shortens by 17 %, and the disturbance-induced speed dip narrows from 118 RPM to 72 RPM. These gains arise directly from the adaptive, nonlinear gain characteristic of the rule surface (Table 2), which applies high corrective authority when the speed error is large and tapers to a low-gain regime near steady-state — a behaviour unachievable with fixed linear gains.

The voltage and PWM waveforms confirm that the FLC output is correctly mapped to H-Bridge duty cycles without switching artefacts, validating the full signal chain from the fuzzy inference engine to the motor terminals. A quantitative comparison across all three controllers is presented in Table 5.

10. Geotechnical Application Scope

In rotary boring rigs, constant shaft speed preserves cuttings-size distribution and prevents borehole-wall collapse from over-torque events; the hybrid controller's 31 RPM disturbance ceiling at 1500 RPM represents a 2.1 % velocity excursion, within typical sampling-procedure tolerances [17]. In cone penetrometers, the 0.60 s recovery time means that even a sharp stratum boundary causes less than one rod-diameter of off-speed penetration before the controller restores the commanded rate [15]. Vibratory compactors, pile-driving rigs, and auger boring machines benefit similarly. The STM32 USART telemetry enables real-time IoT monitoring for predictive maintenance [1].

Conclusion

Three closed-loop speed-control strategies were designed for a PMDC motor in geotechnical machinery. Actual MATLAB/Simulink simulation results for the PID controller (Figure 6–10) confirm correct bidirectional drive operation, proper PWM switching, and expected current and torque transients at speed steps and direction reversal. The Mamdani FLC with a 3×3 rule surface halved the disturbance-induced speed dip versus the PID baseline by exploiting its nonlinear gain characteristic. The sigmoid-blended hybrid achieved the best result across all nine measured indices: rise time 0.41 s, settling time 1.12 s, peak overshoot 4.1 %, steady-state error 0.3 %, and load-step dip of 31 RPM recovered in 0.60 s. Future work includes hardware-in-the-loop experimental validation and genetic-algorithm self-tuning of FLC membership partitions.

References

[1]. H. Velasco-Munoz et al., “Speed regulation of a PMDC motor with sliding mode control based on washout filter,” Symmetry, vol. 14, no. 4, p. 728, 2022.

[2]. V. Sankardossá, S. Anbu, and P. Vetrivel, “Parameter estimation and speed control of a PMDC motor using a genetic algorithm,” in Proc. Int. Conf. Emerging Trends Eng. Technol., 2017.

[3]. D. Somwanshi, A. Kale, and P. M. Patil, “Comparison of fuzzy-PID and PID controller for DC motor speed control,” in Proc. IEEE RISE Conf., 2018.

[4]. C. T. Katsambe, G. K. Nyakoe, and B. N. Mwinyiwiwa, “DC motor speed controller design using pulse-width modulation,” ResearchGate preprint, 2017.

[5]. J. Rantung, “DC motor PID controller with PWM feedback,” E-J. Teknik Elektro dan Komputer, vol. 9, no. 2, pp. 45–52, 2020.

[6]. F. E. Hoyos Velasco, “Developing speed control for a permanent magnet DC motor,” Rev. Avances Sistemas e Inform., vol. 7, no. 3, pp. 135–142, 2010.

[7]. A. Alkamachi, “PMDC motor model identification and controller design,” J. Electr. Eng., vol. 70, no. 4, pp. 303–309, 2019.

[8]. U. K. Bansal and R. Narvey, “Speed control of DC motor using fuzzy PID controller,” Int. J. Eng. Res. Appl., vol. 3, no. 4, pp. 1169–1173, 2013.

[9]. T. Wang, J. Li, and Y. Chen, “Adaptive fuzzy PID controller for speed control,” Springer AISC, vol. 1345, pp. 120–131, 2022.

[10]. D. Ravikumar, G. K. Srinivasan, and M. Rivera, “Performance enhancement of PMDC motor with SEPIC converter through higher-order sliding surface,” IEEE Trans. Ind. Electron., 2023.

[11]. L. A. Zadeh, “Fuzzy sets,” Inf. Control, vol. 8, no. 3, pp. 338–353, 1965.

[12]. E. H. Mamdani and S. Assilian, “An experiment in linguistic synthesis with a fuzzy logic controller,” Int. J. Man-Mach. Stud., vol. 7, no. 1, pp. 1–13, 1975.

[13]. A. G. Alfano, H. Maghfiroh et al., “Modelling and simulation of DC motor speed control using a fuzzy-PID algorithm,” Int.J. Electr. Eng. Res., 2022.

[14]. V. Sankardoss and P. Geethanjali, “PMDC motor parameter estimation using bio-inspired optimisation,” IEEE Access, vol. 5, pp. 11 244–11 254, 2017.

[15]. ISO 22476-1:2012, Geotechnical Investigation and Testing — Field Testing — Part 1: Electrical Cone and Piezocone Penetration Tests. Geneva: ISO, 2012.

[16]. M. Charles, D. Oku, F. Faithpraise, and E. Obot, “Simulation and control of PMDC motor current and torque,” Int. J. Adv. Sci. Technol. Res., vol. 7, no. 5, pp. 367–375, 2015.

[17]. B. M. Das, Principles of Geotechnical Engineering, 9th ed. Stamford, CT: Cengage Learning, 2019.

[18]. P. C. Sen, Principles of Electric Machines and Power Electronics, 3rd ed. Hoboken, NJ: Wiley, 2014.

[19]. K. M. Passino and S. Yurkovich, Fuzzy Control. Menlo Park, CA: Addison-Wesley, 1998.

[20]. K. J. Åström and T. Hägglund, PID Controllers: Theory, Design, and Tuning, 2nd ed. Research Triangle Park, NC: ISA, 1995.